Journal of Nuclear Materials 607 (2025) 155695

Contents lists available at ScienceDirect

Journal of Nuclear Materials

journal homepage: www.elsevier.com/locate/jnucmat

Origins of radiation-induced optical attenuation in neutron-irradiated single-crystal sapphire at elevated temperatures

Yan-Ru Lin, Sabrina Calzada, Chad M. Parish, Christian M. Petrie *

Oak Ridge National Laboratory, P.O. Box 2008, Oak Ridge, TN, USA, 37831

ARTICLE INFO

Keywords:
Optical fibers
Sapphire
Radiation-induced attenuation
Neutron irradiation
Transmission electron microscopy
Voids

ABSTRACT

Sapphire (α-Al_2O_3) is a candidate fiber-optic sensor material for extreme temperature environments, potentially including those of nuclear reactors. However, its optical transmission under high-dose neutron irradiation is not well understood compared with that of conventional fused silica. This study examined dimensional changes, optical transmission, and irradiation-induced defects in neutron-irradiated α-Al_2O_3 at temperatures of 298 °C to 688 °C and doses of 3.2 to 12 dpa. Although previous studies attributed radiation-induced attenuation (RIA) at the highest irradiation temperatures to increased optical scattering from radiation-induced voids, our findings indicate that scattering from neither voids nor dislocation loops can explain the measured attenuation. Instead, absorption due to aluminum vacancy centers appears more likely based on a comparison of the spectral features of the measured optical attenuation with previous literature. Significant *c*-axis swelling (5.51 % ± 0.83 %) was observed in the 12 dpa, 592 °C irradiated sample, much higher than earlier measurements, suggesting temperature sensor drift of 543 °C to 1,140 °C. Void patterning was predominantly observed along the *a*-axis, differing from previous studies on polycrystalline samples, which showed *c*-axis patterning. Dislocation loops evolved into network dislocations with increasing temperature and dose; voids formed within these structures, showing no size or density changes, indicating an atypical growth mechanism.

1. Introduction

Single-crystal sapphire (α-Al_2O_3) is a candidate fiber-optic sensor material for extreme temperature applications beyond the limitations of conventional fused silica fibers [1]. Sapphire fiber-based sensors have measured temperatures as high as 1500 °C using inscribed Bragg gratings that could enable spatially distributed measurements under these extreme conditions [2–5]. These developments have motivated the potential extension of sapphire fiber-based sensors to nuclear energy applications, which offer the unique combination of high temperatures and radiation damage. Radiation effects on α-Al_2O_3 have been the subject of many studies over the years [6–12]. However, of those previous studies, few have reported the optical properties of single-crystal sapphire subjected to the displacement damage levels that would be expected at locations near the fuel within nuclear reactors, for which sapphire optical fibers would be most effective.

The primary limitation for any optical fiber-based sensor for nuclear reactor applications is the attenuation of the light signal that is transmitted through the fiber [13]. In addition, for some sensors that rely on measuring thermomechanical strain in the fiber, radiation-induced dimensional changes cannot be separated from the desired measurand and therefore cause undesired sensor drift [14]. Radiation-induced attenuation (RIA) in sapphire was shown to be quite low (on the order of 1 decibel per meter) at a typical sensing wavelength of 1550 nm following irradiation to a low total neutron fluence, on the order of 10^{17} n/cm^2 [15]. Moreover, similar reactor irradiation tests performed while a portion of the fiber was being heated showed that the RIA decreased monotonically with increasing temperature and that the rate of increase

---

* Corresponding author at: Oak Ridge National Laboratory, P.O. Box 2008, Oak Ridge, TN 37831.
E-mail addresses: liny@ornl.gov (Y.-R. Lin), calzadase@ornl.gov (S. Calzada), parishcm@ornl.gov (C.M. Parish), petriecm@ornl.gov (C.M. Petrie).

https://doi.org/10.1016/j.jnucmat.2025.155695
Received 25 November 2024; Received in revised form 8 January 2025; Accepted 10 February 2025

in RIA approached zero at temperatures in the range of 600 °C to 1000 °C [16].

Irradiation of bulk sapphire samples to a much higher fast neutron fluence (2.4×10^{21} n/cm^2) at temperatures < 300 °C resulted in higher RIA, but the magnitudes and the spectral features were generally similar to those described in the literature [17,18]. In contrast, the RIA following high-dose irradiation at a temperature of 688 °C was found to be prohibitively large, with values on the order of thousands to tens of thousands of decibels per meter, after extrapolating from ~millimeter-length samples to ~meter-length optical fibers. The large RIA was attributed to Rayleigh scattering losses that occur when the propagating light photons encounter voids (presumably radiation-induced) with a much lower refractive index (unity) [17]. This hypothesis was partially based on previous observations of such radiation-induced voids that formed in polycrystalline alumina under similar irradiation doses and temperatures [8,19]. Previous studies [9,19–21] reported that α-Al_2O_3 irradiated at 652 °C to 827 °C experiences significant void swelling (1 % to 5 %) at fluences of 1×10^{21} to 3×10^{22} n/cm^2 (1 dpa to 30 dpa), in contrast to a single-crystal $MgAl_2O_4$ spinel that forms only isolated dislocation loops that do not unfault. Sickafus [6] suggested that the α-Al_2O_3 swelling is attributed to the unfaulting of interstitial dislocation loops and the formation of dislocation networks, which act as sinks for interstitial atoms, leaving a supersaturation of unpaired vacancies in the bulk.

The objective of this work is to test the hypothesis that radiation-induced voids in sapphire are responsible for previously observed RIA at high irradiation dose and temperature by performing transmission electron microscopy (TEM) on similar irradiated samples. The microstructural features were used as inputs to previously established analytical expressions to estimate contributions to scattering losses and are compared with the measured RIA. The results are discussed in terms of implications for sapphire optical fiber-based sensors for extreme-temperature nuclear reactor applications as well as other potential applications of sapphire under the tested dose and temperature regime.

2. Methods

2.1. Materials and irradiation conditions

Single-crystal sapphire samples with nominal dimensions of 16 mm length, 5 mm width, and 0.9 mm thickness were purchased from Kyocera (Fig. 1). The crystals were grown with the *c*-axis oriented along the thickness of the samples. The pre-irradiation densities were measured to be 3.912 ± 0.016 g/cm^3 [17]. The samples were irradiated under an average thermal (energy < 0.5 eV) neutron flux of 1.9×10^{15} n/cm^2•s and an average fast (energy > 0.1 MeV) neutron flux of 1.1×10^{15} n/cm^2•s in the High Flux Isotope Reactor (HFIR) at Oak Ridge National Laboratory (ORNL). The sample identifiers, irradiation temperatures, fast neutron fluences, and damage levels of the three samples selected for TEM analysis are summarized in Table 1. As described in a previous work [17], the sample temperatures were determined based on post-irradiation dilatometric analyses [22] of passive SiC temperature monitors that were co-located with the samples. The directional dimensional changes, also reported in Table 1, were determined by using a micrometer to record changes in the length (*a*-axis) and thickness (*c*-axis). The dimensional changes and their uncertainties were determined by calculating the means and standard deviations, respectively, across the four samples that were irradiated under each condition (12 total samples). In other words, the swelling reflects the distribution of values measured for multiple samples tested under the same conditions, instead of the values measured for the individual samples identified in Table 1. The standard deviations were lower for the *a*-axis data because of the larger sample length compared to its width and the fact that the pre-irradiation thickness was only recorded to within two decimal places (in millimeters), whereas three-decimal precision was used for all other dimensions.

2.2. Optical transmission measurements

The optical transmission data were previously reported for two of the three samples that were characterized via TEM (S12 and S20) [17]. Optical transmission was measured in the third sample (S15) following the same procedure. The results are included later in the discussion of RIA origins (Sections 4.3 and 4.4). Briefly, the outputs from fiber-coupled deuterium and tungsten-halogen light sources were

Table 1
Irradiation conditions and directional dimensional changes of neutron-irradiated single-crystal α-Al_2O_3 samples.

Sample ID	Irradiation temperature (°C)	Fast neutron fluence (n/cm^2)	Dose (dpa)	Swelling (%)	
				a-axis	*c*-axis
S12	298	2.4×10^{21}	3.2	0.42 ± 0.03	1.10 ± 0.64
S15	592	9.6×10^{21}	12	1.33 ± 0.03	5.51 ± 0.83
S20	688	2.4×10^{21}	3.2	0.63 ± 0.04	−0.04 ± 0.72

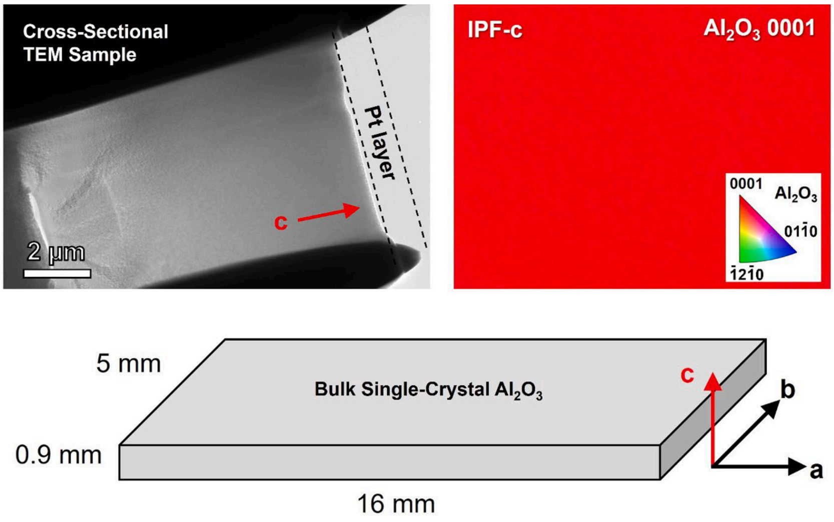

Fig. 1. Geometry, dimensions, and crystal orientation of the (0001) single-crystal α-Al_2O_3 bulk material.

combined using a fiber-optic coupler and were passed through a cuvette holder, within which the samples were held in a custom sample holder. The transmitted light was measured by a pair of spectrometers covering the ultraviolet to near-infrared wavelengths (190 to 1700 nm). Multiple measurements were made with and without a sample inserted to allow for the calculation of statistical uncertainties of the relative transmission after the sample was inserted. The measured wavelength-dependent intensity ratios were converted to optical densities (ODs) using a base 10 logarithm and were divided by the sample thickness to give units of inverse centimeters.

2.3. TEM and sample preparation

TEM samples of neutron-irradiated single-crystal α-Al_2O_3 were prepared using an FEI Versa3D Dual Beam focused ion beam (FIB) scanning electron microscope (SEM) at the Low Activation Materials Development and Analysis facility at ORNL. To reduce charging effects during FIB processing, a 30 to 40 nm carbon layer was coated on the surface of each bulk sample using a Cressington 208C carbon coater equipped with a thickness monitor, as confirmed by electron backscatter diffraction (Fig. 1). Subsequently, a gas injection system was used to deposit a ~2 μm protective Pt layer by releasing a precursor gas that reacts with the ion beam during FIB milling. A TESCAN MIRA3 SEM was used to orient the Al_2O_3 single-crystal with the (0001) plane parallel to the carbon-coated and Pt-deposited surface. Thus, during cross-sectional TEM-FIB sample preparation, the *c*-axis [0001] was perpendicular to the Pt layer. A 30 kV Ga ion beam was used for FIB sample trenching, with the voltage gradually reduced to 15 kV and subsequently to 7 kV for thinning and lift-out. The final polishing of the foils was carried out using 5 kV and 2 kV Ga ions. For the TEM analysis, the FIB sample was tilted along the direction perpendicular to the *c*-axis [0001] to a low-index zone to distinguish dislocation loop information from the *a* and *c* planes. The CrystalMaker SingleCrystal 5 software was used to auto-index the diffraction pattern and to determine the orientation of the crystal. For ease of crystal plane identification, the four-index Miller-Bravais indices (*hkil*) for the hexagonal system were transformed into three-index Miller indices (*hkl*).

Dislocations, dislocation loops, and cavities were characterized using a JEOL JEM-2100F TEM operated at 200 kV. A weak-beam dark-field (WBDF) scanning transmission electron microscopy (STEM) technique [23] was employed with g vectors aligned parallel to the *a*- and *c*-axes to identify *a*-type prism loops and *c*-type basal loops. Voids were examined using the underfocus–overfocus technique with Fresnel contrast. For microstructures with varying sizes, a weighted average size was

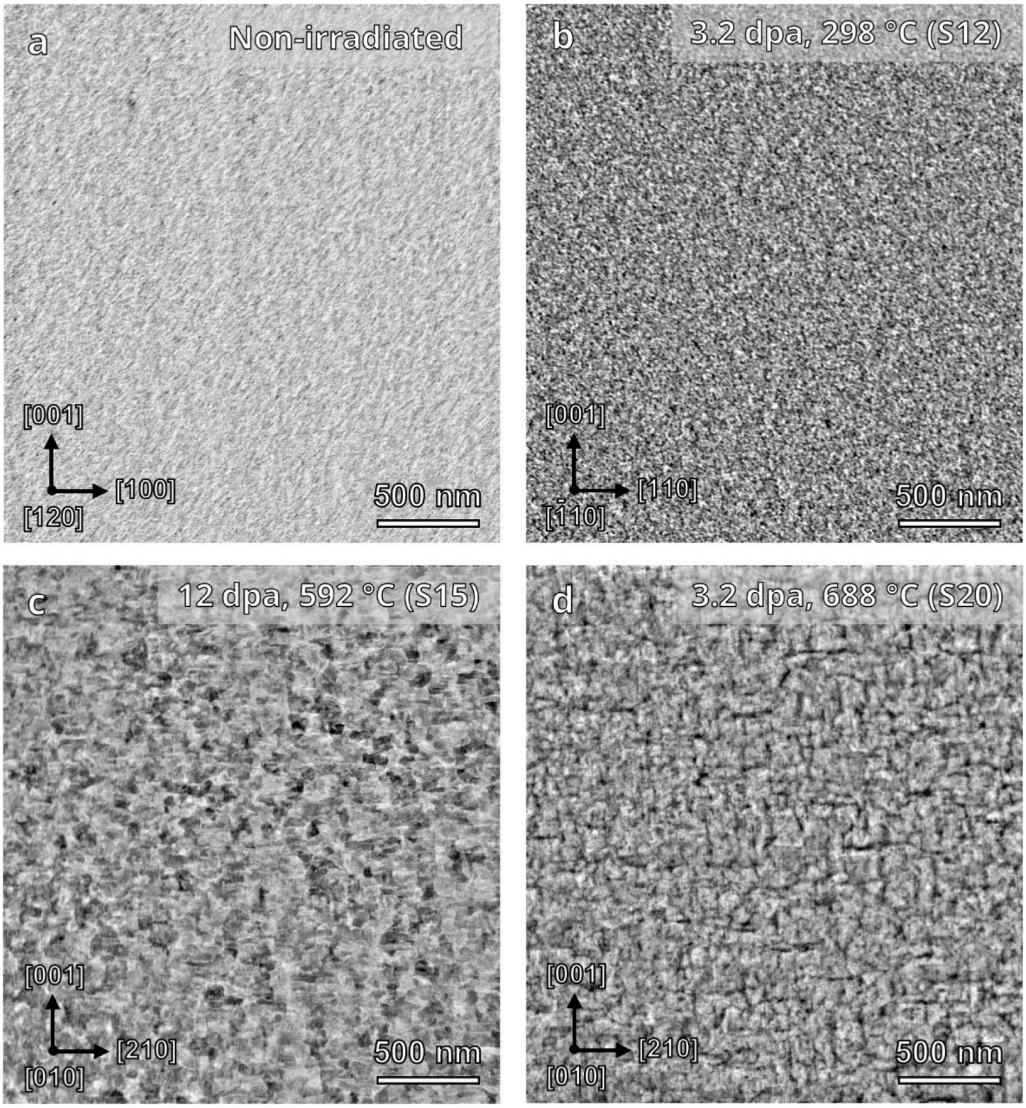

Fig. 2. On-zone STEM-BF images of nonirradiated and neutron-irradiated Al_2O_3: (a) nonirradiated, $Z = [120]$; (b) 3.2 dpa, 298 °C, $Z = [\bar{1}10]$; (c) 12 dpa, 592 °C, $Z = [010]$; and (d) 3.2 dpa, 688 °C, $Z = [010]$.

calculated based on the relative frequency distribution. Dislocation density ρ was calculated from the STEM images using the line-intercept method, following $\rho = 2N/Lt$, where N is the number of intersections between dislocations and randomly drawn lines, L is the total length of the lines, and t is the thickness of the FIB sample. The thicknesses of the FIB samples were estimated using the electron energy loss spectroscopy log-ratio method [24] to allow for quantification of the volume density of the irradiation-induced microstructures.

3. Results

3.1. Dislocation networks and dislocation loops

Fig. 2 presents relatively low-magnification on-zone STEM bright field (BF) images of the nonirradiated and neutron-irradiated single-crystal α-Al_2O_3 samples. The images were rotated to position the Pt surface perpendicular to the *c*-axis and to orient the *c*-axis vertically. The zone axes of Fig. 2a–c, and d were [120], [$\bar{1}$10], [010] and [010], respectively. Dislocation loops were observed in sample S12 (3.2 dpa, 298 °C), whereas dislocation networks dominated in sample S15 (12 dpa, 592 °C) and sample S20 (3.2 dpa, 688 °C). Small black dot defects were also seen in the non-irradiated sample, likely caused by FIB damage, suggesting that some of the black dot contrasts in the STEM-BF images of the neutron-irradiated samples may be artifacts rather than effects of neutron irradiation. Dislocation lines were not observed in the non-irradiated sample.

The WBDF-STEM method was employed to quantify the dislocation loops and to differentiate between basal (*c*) loops and prismatic (*a*) loops. Images were taken along two different g vectors: one parallel to the *c*-axis, where only *c*-loops are visible, and the other perpendicular to the *c*-axis, where only *a*-loops are visible. The loops exhibit bright contrast in WBDF-STEM images, which is the inverse of the dark contrast seen in STEM-BF images. For the unirradiated sample (Fig. 3), the contrast was low in both WBDF-STEM images with $g = [001]$ and $g = [110]$ (with $Z \sim [\bar{1}10]$), showing no obvious dislocations or dislocation loops.

Dislocation loops and lines were observed in all three neutron-irradiated samples: 3.2 dpa at 298 °C (S12), 12 dpa at 592 °C (S15), and 3.2 dpa at 688 °C (S20) (Figs. 4–6). When the WBDF-STEM images were compared with $g = [001]$ (*c*-loops visible) and *g* perpendicular to [001] (*a*-loops visible), a higher density of dislocations and loops was observed with $g = [001]$ across all three neutron irradiation conditions, thus indicating the dominance of *c*-loops formed on the basal plane. For all WBDF images, the samples were first tilted to the on-zone axis and then were tilted less than 7° to a (g, $3g$) weak-beam condition with $S > 0$ for imaging. All STEM-BF and WBDF images in Figs. 4–6 were rotated to position the Pt surface perpendicular to the *c*-axis and the *c*-axis oriented vertically (pointing upward).

Dislocation loop size, loop density, and dislocation density were quantified from STEM images (Figs. 4–6) and are summarized in Table 2. In general, the dislocation density and loop size increased, while the dislocation loop density decreased with increasing temperatures from 298 °C to 688 °C. At 592–688 °C, network dislocations were the predominant defect type, and an increase in damage levels from 3.2 to 12 dpa appeared to have minimal impact on dislocation density. Dislocation density was calculated from STEM-BF images using the line-intercept method, whereas loop size and density were determined from WBDF-STEM images; only dot- and plate-like features were considered loops. Due to the high density of dislocation networks in S15 and S20, it was difficult to clearly discern dislocation loops and lines in some cases, which may have resulted in an overestimation of loop density. Dislocation lines were observed in the S12 sample (3.2 dpa at 298 °C) with a relatively low density of 1.0×10^{13} m^{-2}. Dislocation networks, likely formed through interactions between dislocation lines and dislocation loops that further developed into cell boundaries, were observed in S15 (592 °C, 12 dpa) and S20 (688 °C, 3.2 dpa). The dislocation densities were similar across the two higher-temperature samples, with values near 3×10^{14} m^{-2}, indicating that there was no significant effect from dose (3.2 dpa and 12 dpa) or temperature (592 °C and 688 °C).

For dislocation loops, both *c*-loops and *a*-loops showed that loop size increased with temperature, whereas loop density decreased. When the samples irradiated to 3.2 dpa at different temperatures were compared (298 °C vs. 688 °C), the *c*-loop size was shown to have increased with

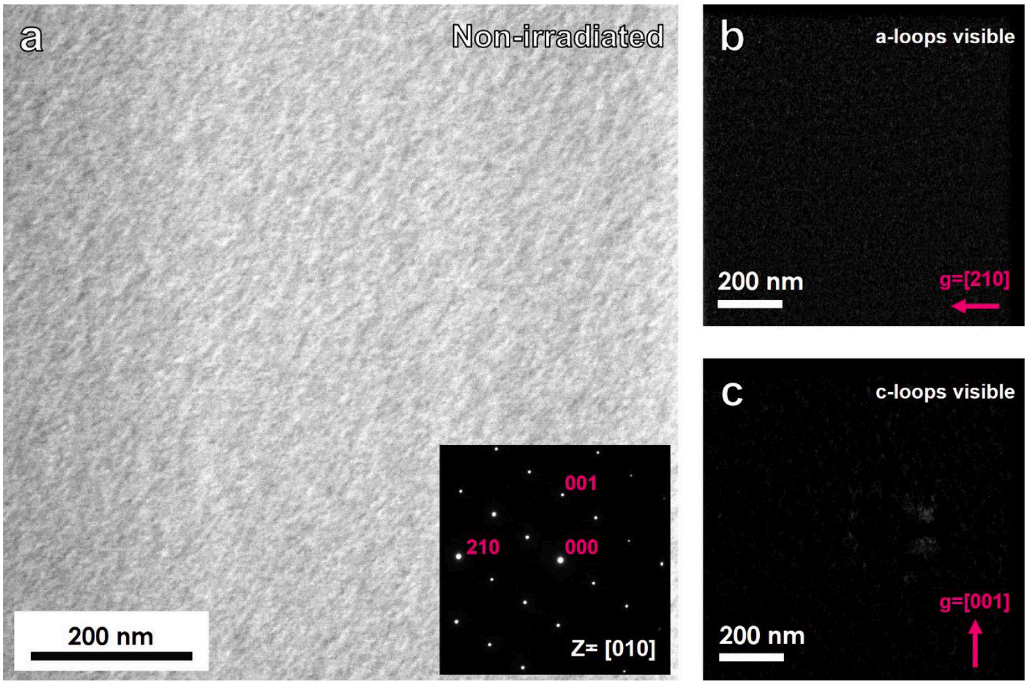

Fig. 3. STEM images of dislocations and loops in nonirradiated Al_2O_3: (a) STEM-BF with $Z = [010]$; (b) WBDF-STEM with $Z \sim [010]$ and $g = [210]$; and (c) WBDF-STEM with $Z \sim [010]$ and $g = [001]$.

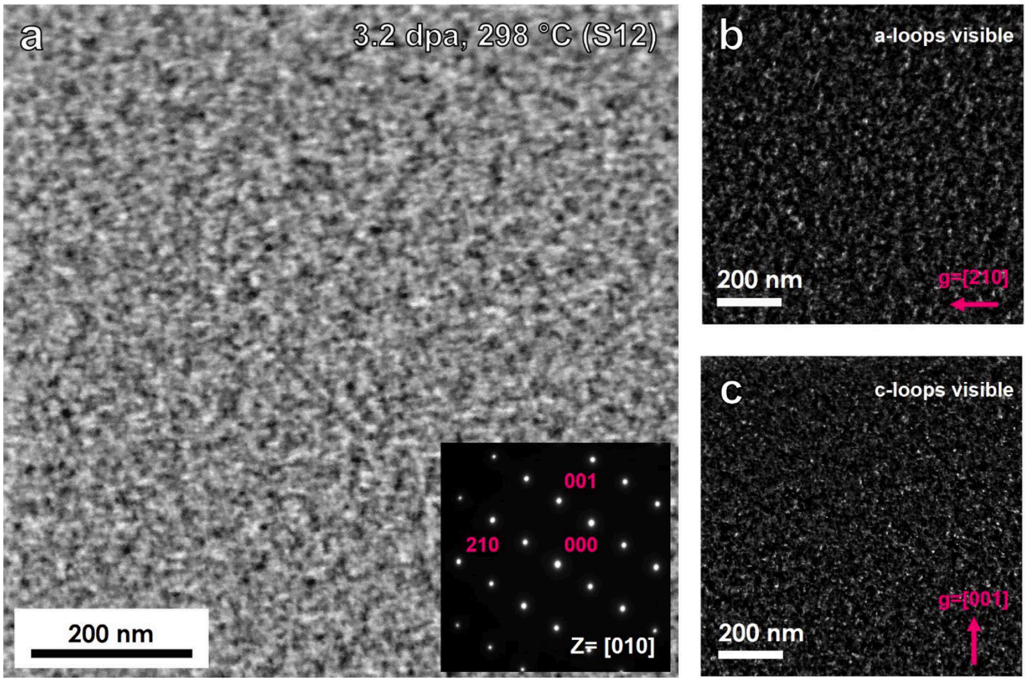

Fig. 4. STEM images of dislocations and loops in neutron-irradiated Al_2O_3 at 298 °C to 3.2 dpa (S12): (a) STEM-BF with $Z \sim [010]$; (b) WBDF-STEM with $Z \sim [010]$ and $g = [210]$; and (c) WBDF-STEM with $Z \sim [010]$ and $g = [001]$.

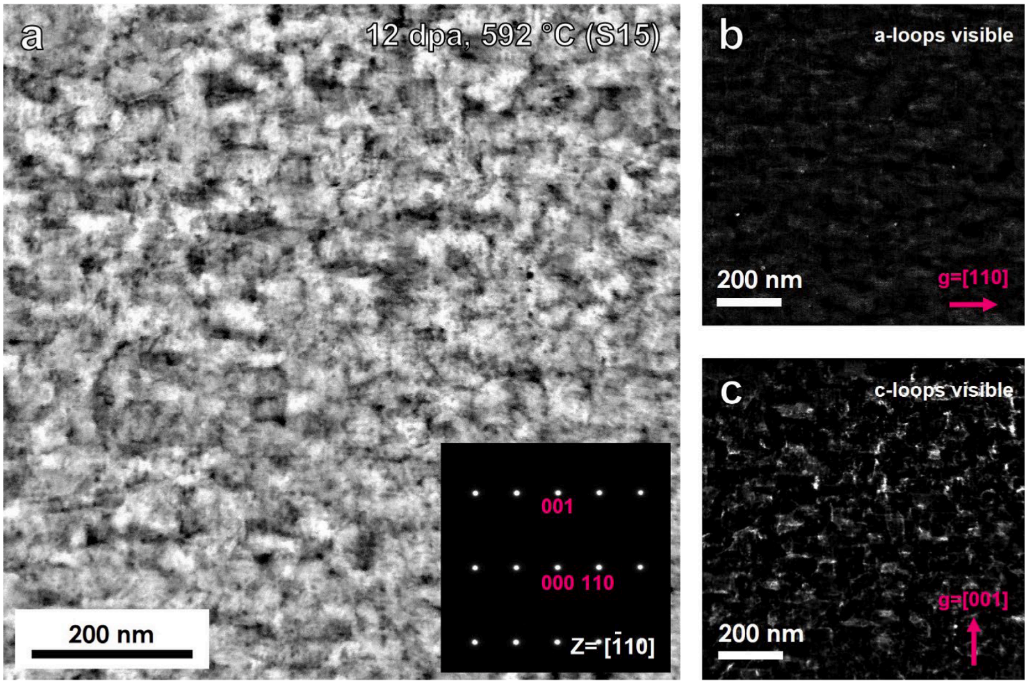

Fig. 5. STEM images of dislocations and loops in neutron-irradiated Al_2O_3 at 592 °C to 12 dpa (S15): (a) STEM-BF with $Z = [\bar{1}10]$; (b) WBDF-STEM with $Z \sim [\bar{1}10]$ and $g = [110]$; and (c) WBDF-STEM with $Z \sim [\bar{1}10]$ and $g = [001]$.

increasing irradiation temperature from 7.2 nm to 62.5 nm, and the *a*-loop size was shown to have increased from 12.5 nm to 28.8 nm. In contrast, the *c*-loop density had decreased from 2.1×10^{22} m^{-3} to 1.2×10^{21} m^{-3}, and the *a*-loop density decreased from 7.4×10^{21} m^{-3} to 7.2×10^{20} m^{-3} as the irradiation temperature increased from 298 °C to 688 °C. The density of *c*-loops was generally higher than that of *a*-loops; loop densities ranged from 7.2×10^{20} m^{-3} to 2.1×10^{22} m^{-3}. Although the average diameter of *c*-loops (7.2 nm) was slightly smaller than that of *a*-loops (12.5 nm) at 298 °C, the average size of *c*-loops increased significantly to 45.3 nm at 592 °C and 62.5 nm at 688 °C. In contrast, the average size of *a*-loops did not change significantly at 592 °C, but it increased to 28.8 nm at 688 °C. For the two high-temperature irradiated samples (688 °C and 592 °C) with low (3.2 dpa) and high (12 dpa) doses, the dose appears to have a weaker effect on loop size and density compared to the effects of temperature.

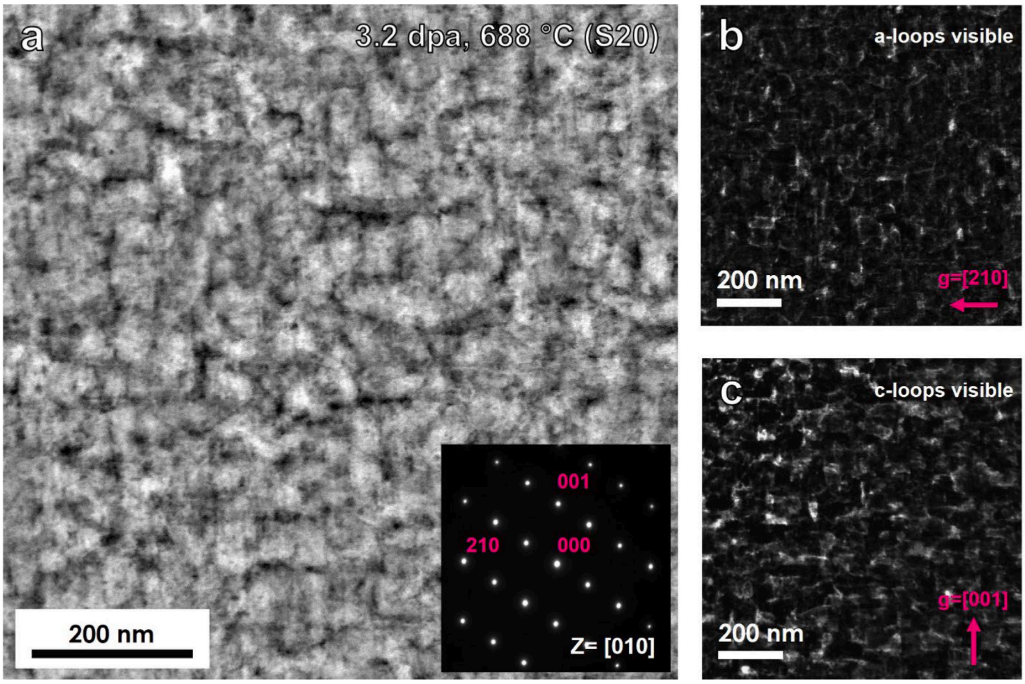

Fig. 6. STEM images of dislocations and loops in neutron-irradiated Al_2O_3 at 688 °C to 3.2 dpa (S20): (a) STEM-BF with $Z \sim [010]$; (b) WBDF-STEM with $Z \sim [010]$ and $g = [210]$; and (c) WBDF-STEM with $Z \sim [010]$ and $g = [001]$.

Table 2
Summary of dislocation and loop characteristics in neutron-irradiated single-crystal α-Al_2O_3 samples at varying temperatures and doses.

Sample ID	Irradiation temperature (°C)	Dose (dpa)	Dislocation density (m^{-2})	*c*-loop		*a*-loop	
				Diameter (nm)	Density (m^{-3})	Diameter (nm)	Density (m^{-3})
S12	298	3.2	1.0×10^{13}	7.2 ± 1.6	2.1×10^{22}	12.5 ± 3.1	7.4×10^{21}
S15	592	12	3.1×10^{14}	45.3 ± 8.9	2.5×10^{21}	13.5 ± 5.6	2.2×10^{21}
S20	688	3.2	2.8×10^{14}	62.5 ± 11.5	1.2×10^{21}	28.8 ± 13	7.2×10^{20}

3.2. Voids

Fig. 7 shows how voids were observed in the neutron-irradiated samples S15 (12 dpa, 592 °C) and S20 (3.2 dpa, 688 °C) but not in sample S12 (3.2 dpa, 298 °C). In the overfocused TEM images shown in Fig. 7 (with a defocus value of approximately 700 nm), voids appear with dark contrast. Void patterning aligned along the *a*-axis was observed in both samples irradiated at the highest temperatures (S15 and S20); no significant differences in void size or density were noted between the two samples. The void sizes were 1.3 nm and 1.4 nm, and the void densities were 1.7×10^{23} m^{-3} and 2.1×10^{23} m^{-3} for S15 and S20, respectively. Unimodal void size distributions were observed in both samples (Fig. 7c).

To confirm the void features, overfocused ($\Delta f = +700$ nm) and underfocused ($\Delta f = -700$ nm) TEM images were taken in which voids appear with dark and bright contrast, respectively (Fig. 8). Regarding the orientation of the void pattern, it was confirmed that the void pattern is oriented along the *a*-axis, which is parallel to the Pt surface layer, because the normal vector of the (0001) single-crystal Al_2O_3 surface is parallel to the *c*-axis. This was further verified using the diffraction pattern and the fast Fourier transform of the high-resolution TEM image (Fig. 8c). In the high-resolution TEM images, spherical voids and voids elongated along both the *a*-axis and the *c*-axis were observed; elongation was predominant along the *a*-axis.

4. Discussion

4.1. Void patterning orientation and dislocation loop type

The void patterning (or void lattice) along the *a*-axis shown in this study differs from the *c*-axis patterning observed by Clinard et al. in their observations of neutron-irradiated polycrystalline Al_2O_3 under similar conditions at 742 °C and 3 dpa [19]. The distribution of dislocations, dislocation loops, and voids were examined to understand why voids in the neutron-irradiated single-crystal Al_2O_3 are arrayed along the *a*-axis. STEM annular dark-field images in Fig. 9a and 9b reveal larger voids and dark contrast forming along dislocation lines or loops aligned with the *a*-axis. TEM underfocused images (Fig. 9c and 9d) show voids assembling in *a*-loops, *c*-loops, and dislocations. The elongated voids along the *a*-axis observed in the high-resolution TEM image (Fig. 8c) are also likely voids within small loops. For the 3.2 dpa at 688 °C condition, voids also accumulated along [111] (or $[11\bar{2}3]$ in hexagonal Miller indices). These observations suggest that the orientation of void patterning and void elongation is influenced by the formation of loops and dislocation networks under neutron irradiation. In this study, the use of single-crystal Al_2O_3 for irradiation may also introduce strain or substrate effects that influence void patterning. In contrast, *c*-axis void patterning was observed in neutron-irradiated polycrystalline Al_2O_3 [19], which involved different initial sink strengths caused by grain boundaries that significantly affect defect evolution and void patterning orientation.

The void size and density (Fig. 7) were similar in samples S15 and S20 (irradiated at 12 dpa, 592 °C and 3.2 dpa, 688 °C, respectively).

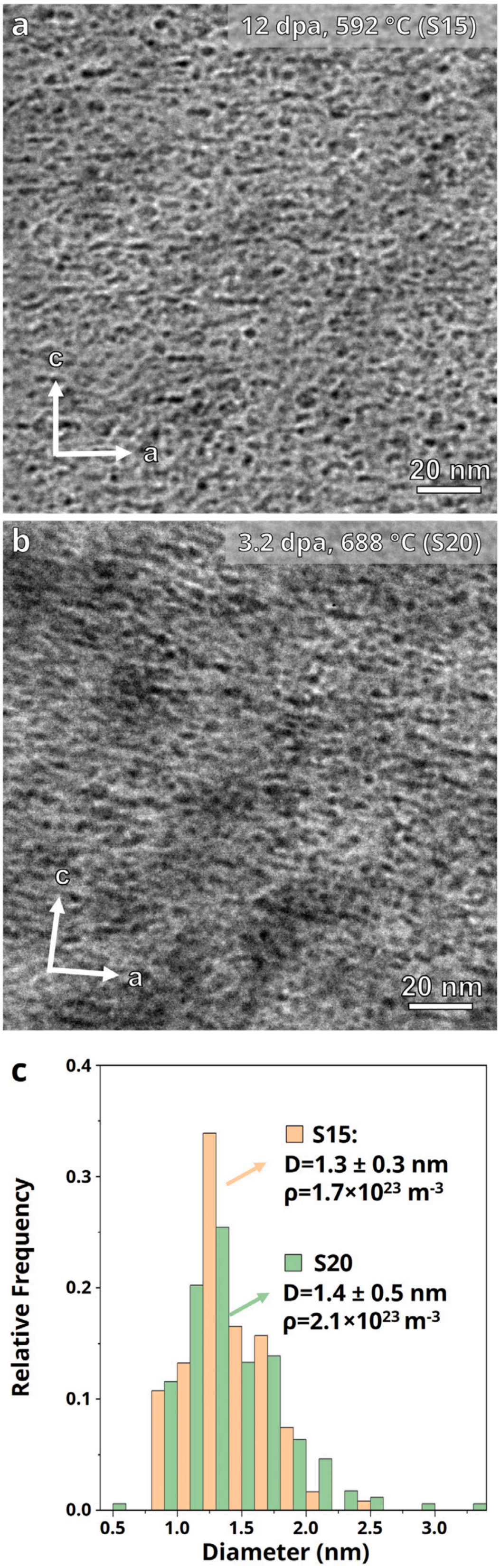

Fig. 7. Overfocused TEM images showing void patterning aligned along the *a*-axis in neutron-irradiated Al_2O_3: (a) 12 dpa, 592 °C; (b) 3.2 dpa, 688 °C; and (c) void size distribution.

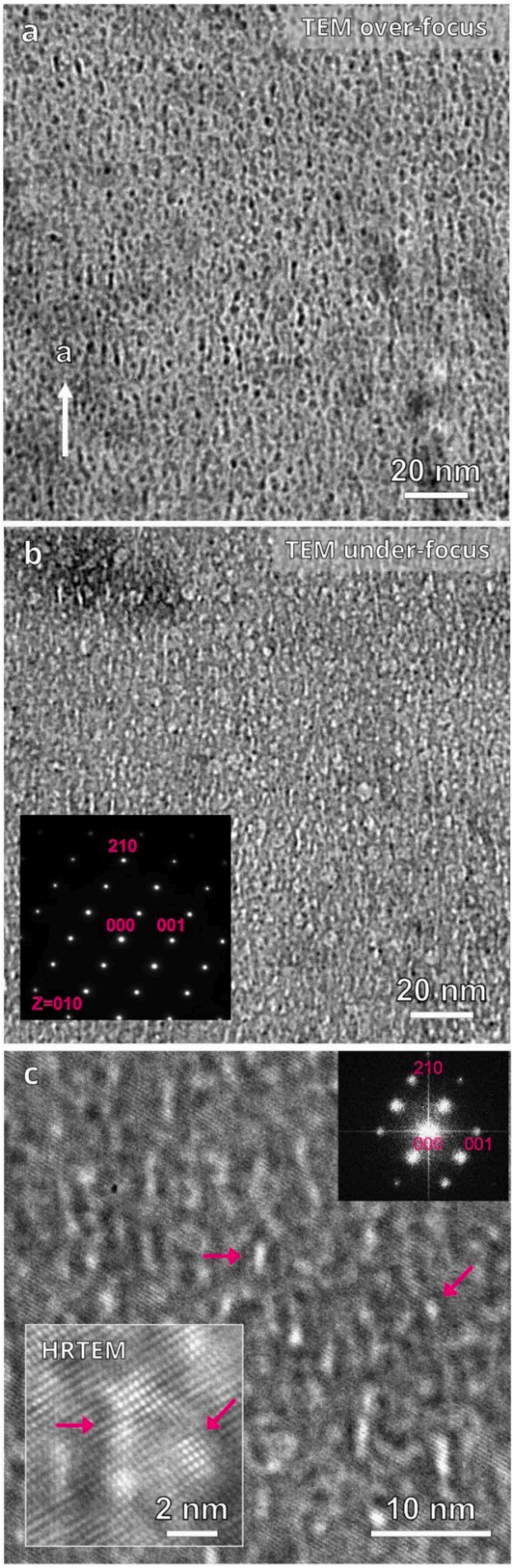

Fig. 8. Voids in neutron-irradiated Al_2O_3 at 592 °C to 12 dpa (S15): (a) overfocused TEM image ($\Delta f = +700$ nm); (b) underfocused TEM image $\Delta f = -700$ nm; and (c) high-resolution TEM image.

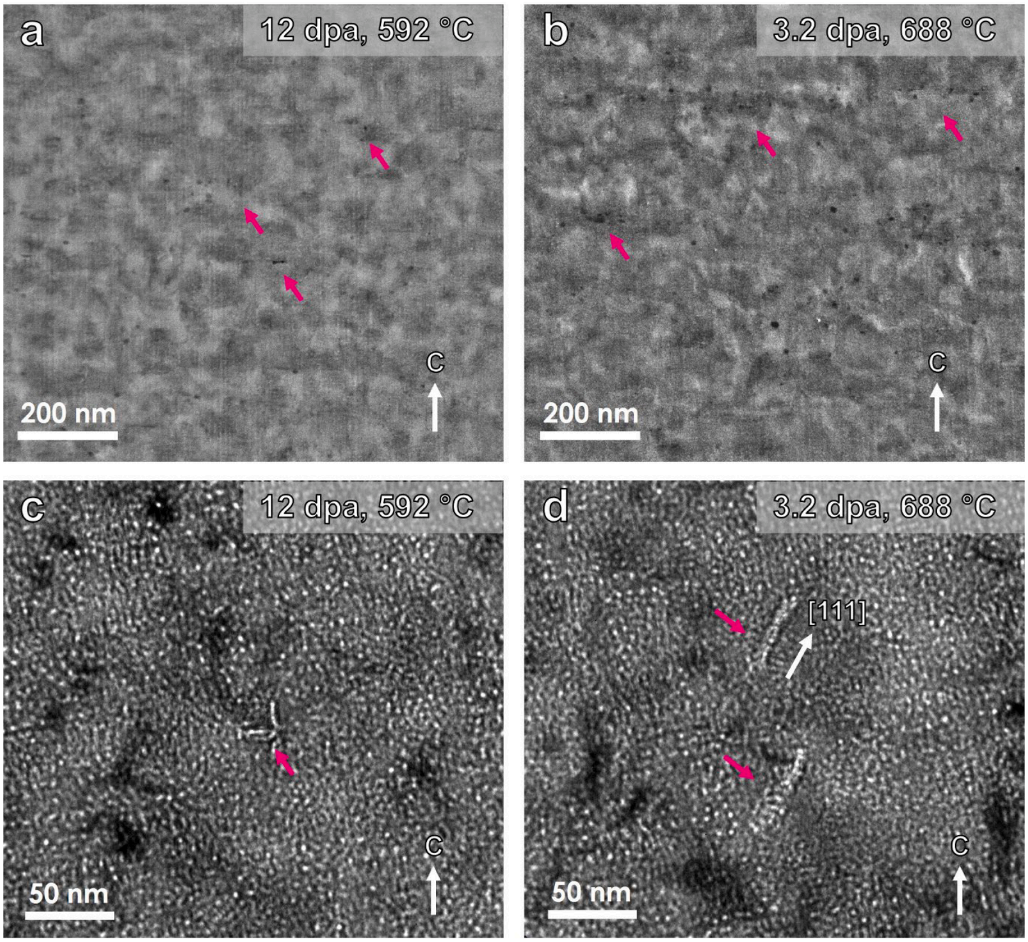

Fig. 9. Void patterning in neutron-irradiated Al_2O_3 at 592 °C to 12 dpa and at 688 °C to 3.2 dpa: (a and b) STEM- annular dark-field images; and (c and d) underfocused TEM images.

Despite one sample having a ~9 dpa higher dose and the other being irradiated at a ~100 °C higher temperature and both having the same dose rate (dpa per second), one might expect larger voids in the 688 °C sample due to the elevated temperature, which typically promotes void growth in irradiated materials [25–27]. However, our observations suggest that the formation of voids is closely related to loops and dislocations. Many voids appear to have nucleated at dislocations and loops, forming distinct void patterns, indicating that the void growth mechanism may differ from that of voids formed in the matrix. It is likely that at temperatures below 1200 °C, where interstitials are significantly more mobile [28], the void formation observed in our study (Fig. 7) is influenced by the presence of interstitial clusters, loops, and dislocation networks, which provide nucleation sites for voids in single-crystal Al_2O_3 with very low initial sink strength. This could also explain the observed *a*-axis void pattern orientation in this study, which deviates from previous studies that reported *c*-axis void patterns [6,19].

The observation of unfaulted loops and dislocation networks (Fig. 4 through 6) is consistent with previous studies under similar neutron irradiation conditions [6]. Large faulted loops were not observed. The prevalence of c-loops on the basal planes appears to account for the predominant *a*-axis void patterning observed in the two Al_2O_3 samples irradiated at high temperatures. The *c*-loops (basal loops) generally dominate for hexagonal ceramics with c/a ratios above the ideal value of 1.63, as summarized in Table 3 (adapted from Ref. [19,29–36]). Similar findings have been reported for high-purity hexagonal close-packed metals [37,38], for which basal plane loop nucleation occurs at $c/a > 1.63$, whereas prism loops form at $c/a < 1.63$. With a c/a ratio of 2.73 for Al_2O_3, which exceeds 1.63, the observed dominance of loops in the basal planes is consistent with previous observations. It has been suggested that, for hexagonal close-packed metals, the principal habit plane for dislocation loop nucleation typically aligns with the most close-packed plane, and this tendency varies with the c/a ratio [39].

Table 3
Loop habit planes for hexagonal ceramic materials. (Modified from Refs. [19, 29–36]).

Material	a (Å)	c (Å)	c/a
Basal loop habit plane			
Ti_3AlC_2	3.07	18.56	6.04
Ti_3SiC_2	3.07	17.68	5.76
6H-SiC	3.08	15.12	4.91
Ti_2AlC	3.06	13.65	4.46
α-Al2O$_3$	4.76	12.99	2.73
Graphite	2.46	6.7	2.72
BeO	2.69	4.38	1.62
AlN	3.11	4.98	1.60
Prism loop habit plane			
ZrB_2	3.18	3.55	1.12
TiB_2	3.02	3.22	1.07

4.2. Rayleigh scattering from voids

The void sizes and densities quantified in Fig. 7 can be used as inputs to previously established analytical models for the optical attenuation that results from Rayleigh scattering. For spherical particles that are small (~nanometer) compared to the wavelength of the scattered light

(~micrometer), the Rayleigh scattering cross section for voids σ_{voids} can be expressed as follows [40]:

$$\sigma_{\text{voids}} = \frac{8\pi}{3}\left(\frac{2\pi n_{\text{med}}}{\lambda}\right)^4 r_{\text{voids}}^6 \left(\frac{m^2-1}{m^2+2}\right)^2 \tag{1}$$

where n_{med} is the refractive index of the bulk medium [41], λ is the vacuum wavelength of light, r_{voids} is the void radius, and m is the ratio of the sphere's refractive index n_{sphere} (unity for voids) to n_{med} ($m = n_{\text{sphere}}/n_{\text{med}}$). The optical attenuation or *OD* of the irradiated samples was previously calculated as follows [17]:

$$OD = -\frac{1}{T}\log_{10}\frac{I}{I_0}, \tag{2}$$

where T is the measured sample thickness, and I and I_0 are the measured optical intensities (as a function of wavelength) with and without the sample inserted, respectively. Contributions to the *OD* resulting from Rayleigh scattering from voids (OD_{voids}) can be calculated using the following equation after converting from base e to base 10:

$$OD_{\text{voids}} = \frac{N_{\text{voids}}\sigma_{\text{voids}}}{\ln(10)}, \tag{3}$$

where N_{voids} is the measured void density (Fig. 7). As will be shown later in Section 4.3, the values for OD_{voids} are on the order of 10^{-8} to 10^{-4} cm^{-1} over the range of wavelengths that were reported previously [17], approximately 300 to 1700 nm. Although the spectral features of Rayleigh scattering losses appeared to match the measured attenuation, as previously reported [17], this appears to be coincedental as the calculated magnitudes do not match the measured values (on the order of tens of inverse centimeters). Therefore, the analysis presented here does not support the previous hypothesis that Rayleigh scattering losses are responsible for the prohibitively large attenuation observed following high-dose irradiation at high temperatures.

4.3. Other scattering mechanisms

It is possible that light is being scattered from other microstructural features besides voids, such as the dislocation loops that were observed in Fig. 2 through 5. Apetz et al. developed a methodology for estimating scattering losses from grain boundaries based on Rayleigh-Gans-Debye theory [42], which is a reasonable approximation for evaluating scattering from dislocation loops. Scattering occurs due to the anisotropy inherent in the hexagonal crystal structure of α-Al_2O_3. This results in a difference in refractive index at the grain boundary (or in this case, dislocation loop).

Similar to voids, the contributions to the *OD* from dislocation loops can be calculated as follows:

$$OD_{\text{loops}} = \frac{N_{\text{loops}}\sigma_{\text{loops}}}{\ln(10)}, \tag{4}$$

where N_{loops} is the measured loop density (see Table 2). When the loop size is much smaller than the wavelength of light (valid in this case), the scattering cross section for loops (σ_{loops}) can be calculated as follows [42]:

$$\sigma_{\text{loops}} = \frac{8\pi^3 r_{\text{loops}}^4}{\lambda^2}\left(\frac{\Delta n}{n_{\text{med}}}\right)^2, \tag{5}$$

where r_{loops} is the loop radius (determined from the diameters in Table 2), and Δn is the difference in refractive index at the grain boundary, or in this case, the dislocation loop. For α-Al_2O_3, the maximum value of Δn is 0.008 [42]. Scattering losses from grain boundaries or dislocation loops involve a λ^{-2} dependence instead of the λ^{-4} dependence for Rayleigh scattering from voids.

Fig. 10 compares the measured *OD* with the calculated values for OD_{loops} and OD_{voids} for each of the samples for which loop or void parameters were determined from TEM images. Because the *c*-loops were generally larger and had higher densities than the *a*-loops, all OD_{loops} data used the parameters from Table 2 for *c*-loops, which would result in a higher *OD*, per Eq. (5). The OD_{loops} data show a range of values

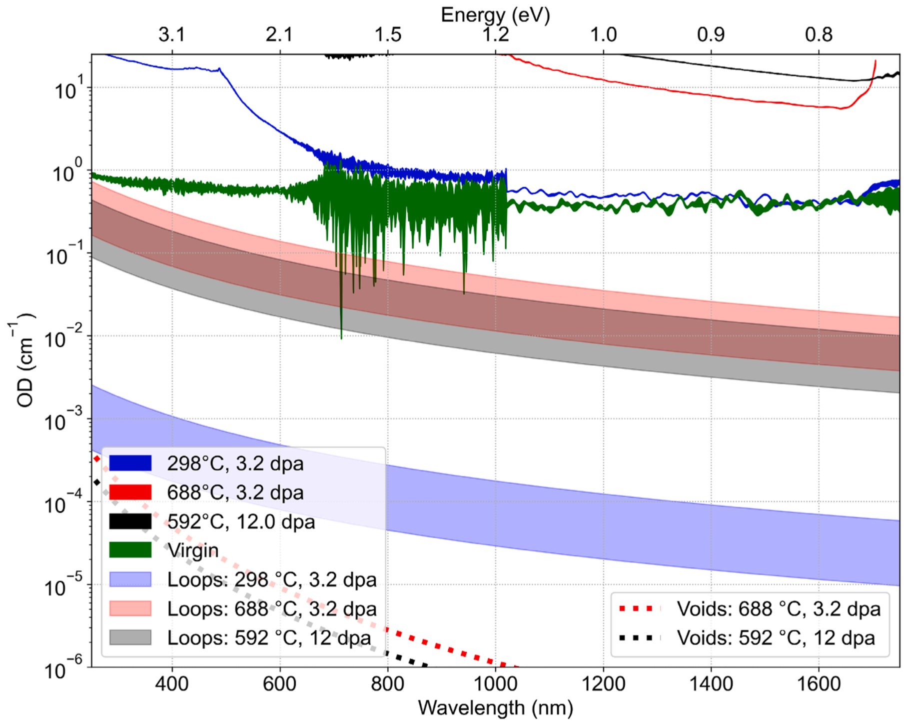

Fig. 10. Comparison of the measured optical densities, some of which were duplicated from a previous work [17], with estimated contributions resulting from scattering from dislocation loops and voids.

corresponding to the uncertainties reported for the loop diameters given in Table 2. As mentioned earlier in Section 2.2, the *OD* measured for two of the three samples was reported previously [17], but the *OD* measured for the sample irradiated at 592 °C to 12 dpa is being reported here for the first time.

Similar to OD_{voids}, the OD_{loops} values that used the measured loop characteristics as inputs (Table 2) are orders of magnitude lower than the measured *OD*. For example, in order for the OD_{loops} curves to increase by three orders of magnitude to align with the measured *OD* curves, the *c*-loops with sizes reported in Table 2 would need to have densities that are three orders of magnitude higher, per Eq. (5). Alternatively, per Eqs. (4) and (5), agreement between the models and measurements would require that *c*-loops with densities reported in Table 2 increase in size by a factor of $1000^{1/4} = 5.6$, to values as high as 350 nm. Loops with these sizes and densities are clearly not observed in the TEM images. These observations imply that optical scaterring losses, regardless of their origins, cannot explain the prohibitively large RIA in sapphire following irradiation at the highest temperatures.

4.4. Alternative optical attenuation mechanisms

If scattering losses cannot explain the significant RIA at the highest irradiation temperatures, then the only other explanation is a large increase in optical absorption. This was not originally considered when the results were first reported [17] because most point defect centers in sapphire absorb over a relatively narrow range of wavelengths and are centered at 450 nm or below [18,43–45]. Table 4 includes a summary of the peak absorption energy (and wavelength) and full width at half maximum (FWHM) of each point defect center that has been identified in the literature. Fig. 11a shows the optical absorption from each point defect center normalized to the peak absorption.

Due to the relatively narrow widths of the most common oxygen vacancy (F) and divacancy (F_2) centers, these defects clearly could not explain the tails in the measured *OD* curves that extend as far as 1600 nm and beyond. A composite aluminum vacancy center (V_{comp}) was previously reported with a broad absorption band near 3 eV (413 nm) and a half width of ~1 eV [48–50]. This defect, previously characterized by Evans and Cain as “weak” when introduced via oxygen ion implantation [48], is associated with positive charge trapped near an aluminum vacancy. It was considered a “composite” defect center because a second absorption band near 5.4 eV (230 nm) was also attributed to this defect. Regardless of the origins of the 5.4 eV band, the broad 3 eV (413 nm) absorption band could potentially explain the long tails in the measured *OD* curves if its intensity were high enough. Moreover, previous density functional theory (DFT) calculations of the optical properties of neutral or negatively charged aluminum vacancies (V or V^{-1}, respectively), predicted large increases in infrared absorption (peak near 2000 nm) [51]. This increased infrared absorption could explain the sharp increases in the measured *OD* at wavelengths > 1600 nm if aluminum vacancy center absorption is indeed responsible for the increases in RIA at the highest irradiation temperatures.

Table 4
Summary of the peak absorption energy and FWHM of each point defect center in sapphire identified in the literature.

Defect	Description	Peak absorption energy (eV) [wavelength]	FWHM (eV)	Reference (s)
F	Neutral O vacancy	6.0 [205 nm]	0.6[1]	[18, 43–45]
F^+	+1 charged O vacancy	5.4 [230 nm] 4.8 [260 nm]	0.32 0.41	[18,44,45]
F_2	Neutral O divacancy	4.1 [300 nm]	0.48[2]	[18,44]
F_2^+	+1 charged O divacancy	3.5 [355 nm]	0.17	[18,44,46]
F_2^{+2}	+2 charged O divacancy	2.8 [450 nm]	0.6[2]	[18,47]
V_{comp}	Composite Al vacancy	3.0 [413 nm]	2.0[1]	[48–50]

[1] FWHM determined from reported half width

[2] FWHM estimated from reported absorption spectra

To test this hypothesis, the tails of the measured *OD* curves were fit to the Gaussian (with respect to energy) V_{comp} absorption band. Fig. 11b shows the results of the fitting compared with the measured *OD* on a linear scale. The data obtained following irradiation at the two highest temperatures were fit over a wavelength range from 1230–1600 nm to focus on the data that were accurately measured while avoiding the increases in *OD* that occurred at higher wavelengths. The data obtained after irradiation at 298 °C were fit over a wavelength range from 500–1000 nm to focus on the tails of the absorption bands that extend into the near infrared while minimizing contributions from defect centers at lower wavelengths. Per Fig. 11a, in addition to the V_{comp} center, the F_2^{+2} center also has some effect on the *OD* near 500 nm. Therefore, the data obtained after irradiation at 298 °C were fit to a sum of two Gaussian absorption bands corresponding to the V_{comp} and F_2^{+2} centers. Finally, the normalized absorption curves for V and V^{-1} centers were plotted alongside the experimental fits to qualitatively show how these related aluminum vacancy centers could be contributing to the measured *OD* at higher wavelengths.

Fig. 11b shows excellent agreement (R^2>0.99) between the fits and the measured *OD* for all irradiation conditions. Per Evans and Cain [48], Smakula’s equation can be used to calculate the aluminum vacancy defect concentration (in cm^{-3}) as $5.8\times 10^{15}\,\frac{\alpha\Delta E}{f}$, where α is the absoprtion at the peak wavelength or energy (in cm^{-1}), ΔE is the half width of the V_{comp} center (1 eV) and f is the oscillator strength (0.15). This gives values of approximately 2×10^{17} cm^{-3} at 298 °C, 3.2 dpa; 2×10^{19} cm^{-3} at 592 °C, 12 dpa; and 7×10^{18} cm^{-3} at 688 °C, 3.2 dpa. These vacancy concentrations are reasonable considering that comparable concentrations of vacancies centers on the order of 10^{17} cm^{-3} were previously observed in amorphous fused silica samples tested under the same conditions as the 3.2 dpa samples evaluated here [52]. Overall, increased absorption from aluminum vacancy centers is a much more likely explanation for the increased RIA in sapphire at the highest irradition temperatures, at least compared with the previous hypothesis regarding increasing optical scattering losses.

4.5. Anisotropic swelling and potential impact on sensor drift

The radiation-induced dimensional changes reported in Table 1 have implications for the drift of many sapphire fiber-based sensors that rely on measuring thermal expansion and thermo-optic effects to demodulate the temperature. Similarly, sapphire fiber-based strain sensors would also be affected by these dimensional changes, which cannot be separated from changes in mechanical strain. Sapphire fibers are grown along the *c*-axis, which means that *c*-axis swelling would have the most significant effect on sensor drift. For these experiments, the primary interest was in measuring optical transmission through the *c*-axis (i.e., along the length of a sapphire fiber). The sample geometry was designed based on compatibility with the HFIR irradiation capsules as well as the ability to measure optical transmission following irradiation. This resulted in a relatively thin geometry, which made it difficult to accurately measure small changes in thickness (*c*-axis swelling) after irradiation. Nevertheless, *c*-axis swelling was measured, albeit with relatively large uncertainties. The *a*-axis swelling was previously reported for two of the three samples [17]. This work reports both *a*- and *c*-axis swelling for all three samples.

The *c*-axis swelling reported in Table 1 for the two samples irradiated to 3.2 dpa is within the range of previously reported values (< 1.7 %) for samples irradiated to fast neutron fluences of the same order of magnitude [17,53–55]. The *a*-axis swelling for the sample irradiated to a fast neutron fluence of 9.6×10^{21} $\mathrm{n/cm}^2$ (12 dpa) at 592 °C is also within

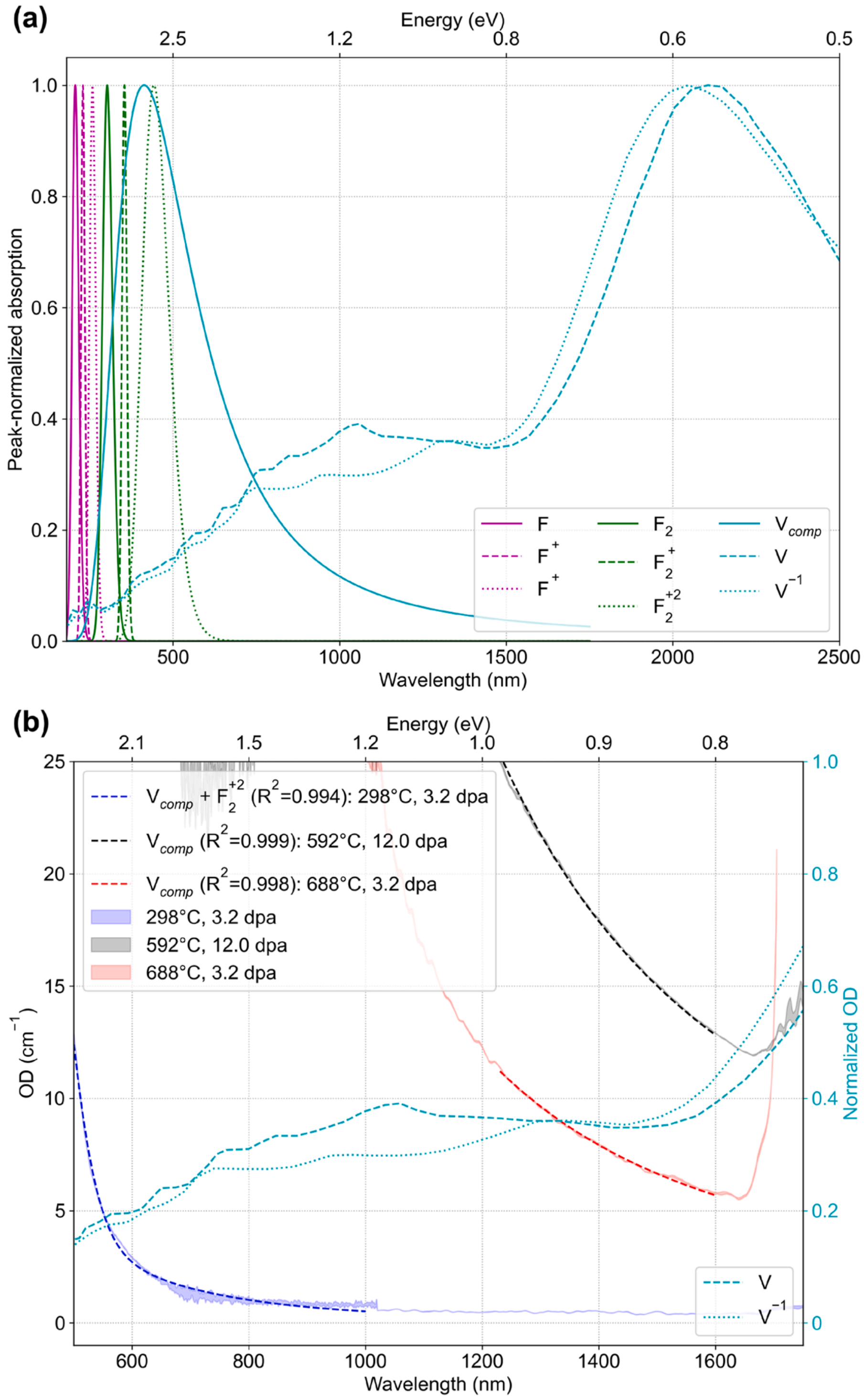

Fig. 11. (a) Normalized optical absorption spectra for various defects identified in the literature, and (b) fitting of the tails of the measured *OD* to the Gaussian (with respect to energy) absorption bands for the V_{comp} and F_2^{+2} defect centers. Normalized absorption from the V and V^{-1} defect centers, determined from previous DFT calculations [51], is plotted in (b) to show qualitatively how these defects could explain the increased *OD* measured at > 1600 nm at the two highest irradiation temperatures.

that same range. However, the *c*-axis swelling for the highest dose sample was significantly higher at 5.51 ± 0.83 %. This larger *c*-axis swelling has important implications for the drift in sapphire fiber-based sensors. When the approach of Petrie et al. [17] was used, the dimensional changes for the 12 dpa, 592 °C sample equated to an estimated sensor drift of 0.87 % to 1.82 % after estimated changes to the refractive index were accounted for. This corresponds to a drift (increase) of 543 °C to 1140 °C for a temperature sensor, assuming that a sensor operating near 1550 nm would exhibit a 25 pm wavelength shift for every 1 °C change in temperature [2]. For comparison, the drift resulting from lower-dose irradiation (∼ 3 dpa) at temperatures ranging from 95 °C to 688 °C was previously estimated to be in the range of −43 °C to −139 °C (temperature decrease). These large differences are attributed to the significantly larger *c*-axis swelling at the higher dose and to the fact that the *c*-axis swelling was measured here instead of being estimated, as in the previous work, based on measured *a*-axis swelling and literature data for the volumetric swelling.

When the dimensional changes in the Al_2O_3 samples irradiated at 12 dpa, 592 °C, are compared with the changes at 3.2 dpa, 688 °C, both the *a*-axis swelling (1.33 % vs. 0.63 %) and *c*-axis swelling (5.51 % vs. −0.04 %) are more pronounced in the 12 dpa, 592 °C samples. Previous studies have shown that the transition temperature between the point defect swelling (or lattice swelling) regime and the cavity swelling regime occurs at about 1000 °C to 1200 °C for Al_2O_3 [56,57]. This suggests that, although voids were observed in both samples (Figs. 7 and 9), point defect clusters (such as dislocation loops or smaller TEM-invisible defect clusters) may still dominate the macroscopic volumetric swelling for the two samples. Zinkle and Pells [57] reported that point defect swelling increased from 2 % to 4.5 % as the dose increased from 1 dpa to 10 dpa at room temperature, supporting our finding that the 12 dpa, 592 °C samples exhibit more swelling than the 3.2 dpa, 688 °C samples. This further indicates that point defect swelling is not saturated at 10 dpa to 12 dpa. Additional studies at irradiation temperatures above 1000 °C would be valuable to determine whether void growth and dimensional changes due to void swelling would significantly affect RIA and sensor drift.

5. Conclusions

The dimensional change, optical transmission, and TEM microstructure analyses reported here provide a more complete picture of radiation effects on single-crystal sapphire materials and their potential application in optical fiber-based sensors for extreme temperature applications in nuclear reactors or other high-radiation environments. The void patterning in neutron-irradiated single-crystal samples (*a*-axis) show significant differences from polycrystalline samples (*c*-axis) that were irradiated under similar conditions. Voids were observed forming in dislocation loops and dislocations, suggesting that void formation along the *a*-axis is linked predominantly to the *c*-loops. Notably, void size and density within the patterning remained relatively unchanged (1.7–2.1 $\times 10^{23}$ m^{-3}) with increasing temperature and dose, deviating from typical void growth behaviors presented in the matrix. Dislocation loops evolved into network dislocations with increasing temperature and dose, a finding that is consistent with previous studies.

Despite observing voids, dislocations and loops following irradiation at temperatures near 600 °C or higher, the previous hypothesis that scattering losses could explain the measured RIA is not supported by the results obtained here. Estimates for the contributions to RIA caused by optical scattering from voids and dislocation loops using the measured defect sizes and densities were at least two orders of magnitude lower than the measured RIA. Alternatively, increased absorption from a composite aluminum vacancy center (V_{comp}) was found to be a much more likely explanation based on fitting the resolvable spectral regions of the measured *OD* to Gaussian absorption bands that were previously identified in the literature. The fits showed excellent agreement with the experimental data, with $R^2 > 0.99$ for all irradiation conditions. The aluminum vacancy concentrations were estimated for each irradiation condition, based on the results of the fits to the measured *OD*, and were found to increase by two orders of magnitude to 2×10^{19} cm^{-3} at 592 °C, 12 dpa, compared with 2×10^{17} cm^{-3} at 298 °C, 3.2 dpa. A relatively smaller increase was observed when the temperature was increased from 298 °C to 688 °C at 3.2 dpa, as the aluminum vacancy concentration was found to be 7×10^{18} cm^{-3} at 688 °C, 3.2 dpa. The increases in the measured *OD* at higher wavelengths (> 1600 nm) qualitatively compare well with previous DFT simulations that predict increased absorption due to neutral or negatively charged aluminum vacancies. Although additional data are required to more clearly understand the dose and temperature trends, we conclude that increased aluminum vacancy absorption is a far more likely origin for the increased RIA following irradiation at 592 and 688 °C compared with increased scattering losses.

Despite the relatively large uncertainties in the measured directional radiation-induced dimensional changes, the *c*-axis swelling of 5.51 % ± 0.83 % in the sample exposed to the highest dose (12 dpa) was found to be significantly higher than previously measured values (< 1.7 %) at lower dose. This swelling would translate to an estimated drift of 543 °C to 1140 °C for a sapphire fiber-based temperature sensor.

CRediT authorship contribution statement

Yan-Ru Lin: Writing – review & editing, Writing – original draft, Methodology, Investigation, Formal analysis, Data curation. **Sabrina Calzada:** Investigation. **Chad M. Parish:** Writing – review & editing, Supervision, Methodology. **Christian M. Petrie:** Writing – review & editing, Writing – original draft, Methodology, Investigation, Formal analysis, Data curation, Conceptualization.

Declaration of competing interest

The authors declare that they have no known competing financial interests or personal relationships that could have appeared to influence the work reported in this paper.

Acknowledgments

The characterization and analysis reported here were supported by the Advanced Sensors and Instrumentation program of the US Department of Energy's Office of Nuclear Energy (DOE-NE). The irradiation experiments were funded by the ORNL Laboratory Directed Research and Development Program, managed by UT- Battelle, LLC, for the US DOE. A portion of this research used the irradiation capabilities of HFIR, a DOE Office of Science User Facility operated by ORNL. The optical transmission measurements were funded by DOE-NE under DOE Idaho Operations Office Contract DE-AC07–051D14517 as part of a Nuclear Science User Facilities rapid turnaround experiment. We gratefully acknowledge the valuable insights from Dr. Steven J. Zinkle of the University of Tennessee, Knoxville. Tony Birri, Travis Dixon, and Kyle Everett (ORNL) assisted with the optical transmission measurements.

Data availability

Data will be made available on request.

References

[1] C. Zhu, R.E. Gerald, J. Huang, Progress toward sapphire optical Fiber sensors for high-temperature applications, IEEE Trans. Instrum. Meas. 69 (11) (2020) 8639–8655.

[2] D. Grobnic, S.J. Mihailov, C.W. Smelser, D. Huimin, Sapphire fiber Bragg grating sensor made using femtosecond laser radiation for ultrahigh temperature applications, IEEE Photonics Technol. Lett. 16 (11) (2004) 2505–2507.

[3] S. Yang, D. Hu, A. Wang, Point-by-point fabrication and characterization of sapphire fiber bragg gratings, Opt. Lett. 42 (20) (2017) 4219–4222.

[4] M. Busch, W. Ecke, I. Latka, D. Fischer, R. Willsch, H. Bartelt, Inscription and characterization of Bragg gratings in single-crystal sapphire optical fibres for high-temperature sensor applications, Meas. Sci. Technol. 20 (11) (2009) 115301.

[5] B.A. Wilson, T.E. Blue, Quasi-distributed temperature sensing using type-II Fiber bragg gratings in sapphire optical Fiber to temperatures up to 1300°C, IEEE Sensors J. 18 (20) (2018) 8345–8351.

[6] K.E. Sickafus, 1.05 - Radiation-induced effects on material properties of ceramics (mechanical and dimensional, in: R.J.M. Konings (Ed.), Comprehensive Nuclear Materials, Elsevier, Oxford, 2012, pp. 123–139.

[7] F.W. Clinard, Ceramics for fusion applications, Ceram. Int. 13 (2) (1987) 69–75.

[8] C. Kinoshita, S.J. Zinkle, Potential and limitations of ceramics in terms of structural and electrical integrity in fusion environments, J. Nucl. Mater. 233-237 (1996) 100–110.

[9] C.A. Parker, L.W. Hobbs, K.C. Russell, F.W. Clinard, Damage structures in fast neutron irradiated magnesium aluminate and electron irradiated aluminum oxynitride spinels, J. Nucl. Mater. 133-134 (1985) 741–744.

[10] V.Y. Yurina, V.V. Neshchimenko, L. Chundong, Optical properties and radiation stability of Al2O3 microparticles, nanoparticles and microspheres, J. Surf. Invest. 14 (2) (2020) 253–259.

[11] D. Gupta, V. Chauhan, N. Koratkar, F. Singh, A. Kumar, S. Kumar, R. Kumar, High energy (MeV) ion beam induced modifications in Al2O3-ZnO multilayers thin films grown by ALD and enhancement in photoluminescence, optical and structural properties, Vacuum 192 (2021) 110435.

[12] V. Chauhan, R. Kumar, Electronic excitation induced modifications in surface morphological, optical and physico-chemical properties of ALD grown nanocrystalline Al2O3 thin films, Superlattices Microstruct. 141 (2020) 106389.

[13] P.F. Kashaykin, A.L. Tomashuk, S.A. Vasiliev, A.D. Ignatyev, A.A. Shaimerdenov, Y. V. Ponkratov, T.V. Kulsartov, Y.A. Kenzhin, S. Kh. Gizatulin, T.K. Zholdybayev, Y. V. Chikhray, S.L. Semjonov, Radiation resistance of single-mode optical fibres with view to in-reactor applications, Nuclear Mater. Energy 27 (2021) 100981.

[14] K. Wang, X. Dong, P. Kienle, M. Fink, W. Kurz, M.H. Köhler, M. Jakobi, A.W. Koch, Optical Fiber sensor for temperature and strain measurement based on multimode interference and square-core Fiber, Micromachines (Basel) 12 (10) (2021).

[15] C.M. Petrie, W. Windl, T.E. Blue, In-situ reactor radiation-induced attenuation in Sapphire optical fibers, J. Am. Ceram. Soc. 97 (12) (2014) 3883–3889.

[16] C.M. Petrie, T.E. Blue, In situ reactor radiation-induced attenuation in sapphire optical fibers heated up to 1000°C, Nucl. Instrum. Methods Phys. Res., Sect. B 342 (2015) 91–97.

[17] C.M. Petrie, A. Birri, T.E. Blue, Optical transmission and dimensional stability of single-crystal sapphire after high-dose neutron irradiation at various temperatures up to 688°C, J. Nucl. Mater. 559 (2022) 153432.

[18] G. Pogatshnik, Y. Chen, B. Evans, A model of lattice defects in sapphire, IEEE Trans. Nucl. Sci. 34 (6) (1987) 1709–1712.

[19] F.W. Clinard, G.F. Hurley, L.W. Hobbs, Neutron irradiation damage in MgO, Al2O3 and MgAl2O4 ceramics, J. Nucl. Mater. 108-109 (1982) 655–670.

[20] C.A. Black, F.A. Garner, R.C. Bradt, Influence of high dose neutron irradiation at 385 and 750°C on the microhardness of MgAl2O4 spinel, J. Nucl. Mater. 212-215 (1994) 1096–1100.

[21] F.A. Garner, G.W. Hollenberg, F.D. Hobbs, J.L. Ryan, Z. Li, C.A. Black, R.C. Bradt, Dimensional stability, optical and elastic properties of MgAl2O4 spinel irradiated in FFTF to very high exposures, J. Nucl. Mater. 212-215 (1994) 1087–1090.

[22] K.G. Field, J.L. McDuffee, J.W. Geringer, C.M. Petrie, Y. Katoh, Evaluation of the continuous dilatometer method of silicon carbide thermometry for passive irradiation temperature determination, Nucl. Instrum. Methods Phys. Res., Sect. B 445 (2019) 46–56.

[23] Y.-R. Lin, Y. Li, S.J. Zinkle, J.D. Arregui-Mena, M.G. Burke, Application of weak-beam dark-field STEM for dislocation loop analysis†, Microsc. Microanal. 30 (4) (2024) 681–691.

[24] T. Malis, S.C. Cheng, R.F. Egerton, EELS log-ratio technique for specimen-thickness measurement in the TEM, J. Electron Microsc. Tech. 8 (2) (1988) 193–200.

[25] Y. Watanabe, K. Morishita, T. Nozawa, H. Tanigawa, Irradiation temperature and dose rate dependence of void swelling in RAFM steel during irradiation: reaction rate theory analysis, Fusion Eng. Des. 194 (2023) 113899.

[26] G.P. Pells, Radiation effects in ceramics, MRS Bull. 22 (4) (1997) 22–28.

[27] Y.-R. Lin, C.-S. Ku, C.-Y. Ho, W.-T. Chuang, S. Kondo, J.-J. Kai, Irradiation-induced microstructural evolution and swelling of 3C-SiC, J. Nucl. Mater. 459 (2015) 276–283.

[28] V.N. Kuzovkov, E.A. Kotomin, A.I. Popov, Kinetics of the electronic center annealing in Al2O3 crystals, J. Nucl. Mater. 502 (2018) 295–300.

[29] A. Bhattacharya, C.M. Parish, T. Koyanagi, C.M. Petrie, D. King, G. Hilmas, W. G. Fahrenholtz, S.J. Zinkle, Y. Katoh, Nano-scale microstructure damage by neutron irradiations in a novel boron-11 enriched TiB2 ultra-high temperature ceramic, Acta Mater. 165 (2019) 26–39.

[30] T. Koyanagi, Y. Katoh, C. Ang, D. King, G.E. Hilmas, W.G. Fahrenholtz, Response of isotopically tailored titanium diboride to neutron irradiation, J. Am. Ceram. Soc. 102 (1) (2019) 85–89.

[31] D.J. Tallman, L. He, B.L. Garcia-Diaz, E.N. Hoffman, G. Kohse, R.L. Sindelar, M. W. Barsoum, Effect of neutron irradiation on defect evolution in Ti3SiC2 and Ti2AlC, J. Nucl. Mater. 468 (2016) 194–206.

[32] D.J. Tallman, E.N. Hoffman, E.a.N. Caspi, B.L. Garcia-Diaz, G. Kohse, R.L. Sindelar, M.W. Barsoum, Effect of neutron irradiation on select MAX phases, Acta Mater. 85 (2015) 132–143.

[33] T. Yano, T. Iseki, High-resolution electron microscopy of neutron-irradiation-induced dislocations in SiC, Philos. Mag. A 62 (4) (1990) 421–430.

[34] T.D. Burchell, 4.10 - Radiation effects in graphite, in: R.J.M. Konings (Ed.), Comprehensive Nuclear Materials, Elsevier, Oxford, 2012, pp. 299–324.

[35] M. Akiyoshi, T. Yano, A new type of defect on {1120} planes in ß-Si3N4 produced by neutron irradiation, Philos. Mag. Lett. 81 (4) (2001) 251–258.

[36] Y.-R. Lin, T. Koyanagi, D.J. Sprouster, C.M. Petrie, W. Fahrenholtz, G.E. Hilmas, Y. Katoh, Response of 11B enriched ZrB2 ultra-high temperature ceramic to neutron irradiation at elevated temperatures, Acta Mater. 276 (2024) 120111.

[37] J. Li, Y. Chen, H. Wang, X. Zhang, In situ study on enhanced heavy ion irradiation tolerance of porous Mg, Scr. Mater. 144 (2018) 13–17.

[38] M. Griffiths, Microstructure evolution in h.c.p. metals during irradiation, Philos. Mag. A 63 (5) (1991) 835–847.

[39] M. Griffiths, Evolution of microstructure in hcp metals during irradiation, J. Nucl. Mater. 205 (1993) 225–241.

[40] A.J. Cox, A.J. DeWeerd, J. Linden, An experiment to measure Mie and Rayleigh total scattering cross sections, Am. J. Phys. 70 (6) (2002) 620–625.

[41] I.H. Malitson, Refraction and dispersion of synthetic sapphire, J. Opt. Soc. Amer. B Opt. Phys. 52 (1962) 1377–1379.

[42] R. Apetz, M.P.B. van Bruggen, Transparent Alumina: A light-scattering model, J. Am. Ceram. Soc. 86 (3) (2003) 480–486.

[43] K.H. Lee, J.H. Crawford, Electron centers in single-crystal Al2O3, Phys. Rev. B 15 (8) (1977) 4065–4070.

[44] S.V. Solov’ev, I.I. Milman, A.I. Syurdo, Thermal- and photo-induced transformations of luminescence centers in αd-Al2O3 anion-defective crystals, Phys. Solid State 54 (4) (2012) 726–734.

[45] B.D. Evans, M. Stapelbroek, Optical properties of the F+ center in crystalline Al2O3, Phys. Rev. B 18 (12) (1978) 7089–7098.

[46] L.S. Welch, A.E. Hughes, G.P. Pells, Polarised luminescence in neutron- and proton-irradiated α-Al2O3, J. Phys. C Solid State Phys. 13 (9) (1980) 1805.

[47] I.K. Abdukadyrova, Effect of neutron irradiation on optical spectra of sapphire crystals, Inorg. Mater. 44 (7) (2008) 721–725.

[48] B.D. Evans, L.S. Cain, A cation vacancy center in crystalline Al2O3, Radiat. Eff. Defects Solids 134 (1-4) (1995) 329–332.

[49] T. Turner, J. Crawford Jr, V centers in single crystal Al2O3, Solid State Commun. 17 (2) (1975) 167–169.

[50] R.H. Bartram, C.E. Swenberg, J.T. Fournier, Theory of trapped-hole centers in aluminum oxide, Phys. Rev. 139 (3A) (1965) A941–A951.

[51] M. Hornak, Energetics, Kinetics, and Optical Absorption of Point Defects in Sapphire, The Ohio State University, 2016.

[52] C.M. Petrie, A. Birri, T.E. Blue, High-dose temperature-dependent neutron irradiation effects on the optical transmission and dimensional stability of amorphous fused silica, J. Non-Cryst. Solids 525 (2019) 119668.

[53] R.S. Wilks, J.A. Desport, J.A.G. Smith, The irradiation-induced macroscopic growth of α-Al2O3 single crystals, J. Nucl. Mater. 24 (1) (1967) 80–86.

[54] R.B. Roof, W.A. Ranken, Radiation effects on the lattice constants of single crystal A12O3, J. Nucl. Mater. 55 (3) (1975) 357–358.

[55] G. Keilholtz, R. Moore, H. Robertson, Effects of Fast Neutrons on Polycrystalline Alumina and Other Electrical Insulators at Temperatures from 60° to 1230°C, ORNL-4678, Oak Ridge National Laboratory, Oak Ridge, TN, 1971.

[56] T. Yano, H. Konishi, S. Yamazaki, M.I.b. Idris, K. Yoshida, Recovery of neutron-irradiation-induced defects of Al2O3, Y2O3, and yttrium-aluminum garnet, J. Nucl. Sci. Technol. 54 (8) (2017) 891–898.

[57] S.J. Zinkle, G.P. Pells, Microstructure of Al2O3 and MgAl2O4 irradiated at low temperatures, J. Nucl. Mater. 253 (1) (1998) 120–132.